PCCP

Probing Spatial Coupling of Resistive Modes in Porous Intercalation Electrodes through Impedance Spectroscopy

SCHOLARONE™
Manuscripts

Probing Spatial Coupling of Resistive Modes in Porous Intercalation Electrodes through Impedance Spectroscopy

Aashutosh N. Mistry[†] and Partha P. Mukherjee[‡]*

School of Mechanical Engineering, Purdue University, West Lafayette, IN 47907, USA

[†] ORCID: $0000 - 0002 - 4359 - 4975$
[‡] ORCID: $0000 - 0001 - 7900 - 7261$

*E-mail: pmukherjee@purdue.edu

Abstract

In porous intercalation electrodes, coupled charge and species transport interactions take place at the pore-scale, while often observations are made at the electrode-scale. The physical manifestation these interactions from pore- to electrode-scale is poorly understood. Moreover, the spatial arrangement of the constituent material phases forming a porous electrode significantly affects the multi-modal electrochemical and transport interplay. In this study, the relation between the electrode specification, resultant porous microstructure, and electrode-scale resistances is delineated based on a virtual deconvolution of the impedance response. Relevant short- and long-range interactions are identified. Without altering the microstructural arrangement, if the electrode thickness is increased, the resistances do not scale linearly with thickness. This dependence is also probed to identify the fundamental origins of thick electrode limitations.

Introduction

The transient electrochemical response of porous intercalation electrodes is a combination of various finite rate interactions taking place at the pore-scale, for example, ionic transport through the electrolyte-filled pore network. The geometrical arrangement of material phases constituting a porous electrode modulates the severity of these interactions, and consequently the electrode-scale response. Thus, the porous intercalation electrodes represent a fascinating electrochemical system where the transient behavior strongly relies on the presence of non-intercalating phases, while the energy storage capacity correlates to the amount of intercalation material[1-10]. Physically the geometrical arrangement (more commonly known as the electrode microstructure) changes as electrode recipe is varied. Given the correlation among pore-scale physicochemical interactions and microstructural arrangement, an "appropriate" electrode recipe should culminate in desired electrochemical behavior. The importance of this connection from recipe to microstructure to performance has been recognized[11-23] however the exact correlation is not clearly understood[24, 25]. Fundamentally, such incertitude is rooted in two closely related questions:

- How do relevant microstructural properties vary with electrode recipe? In recent years, advanced imaging studies have provided quite a few detailed insights into active particles and their arrangement, however, sufficient visualization of electrolyte and carbon-binder network is challenging[26] and makes a correlation between recipe and microstructure difficult to ascertain.

- How do different pore-scale interactions convolve to electrode-scale, i.e., observable, electrochemical response? Porous electrodes gradually convert ionic current (porosity and tortuosity are relevant descriptors) into electronic via electrochemical reaction (relates to

the active area). Thus, at different locations in an electrode, the relevance of the associated resistive modes is dissimilar[24].

Authors have recently developed accurate microstructural reconstructions for composite porous electrodes containing all the essential material phases[24] (verified against relevant experiments). Such investigations[24, 27] delineate the electrode recipe variations in terms of effective microstructural properties. The present study establishes reciprocity among pore-scale interactions, their geometrical descriptors and electrochemical complexations as measured via impedance spectroscopy.

Electrochemical Impedance Response of a Porous Electrode

Impedance spectroscopy probes electrode-scale electrochemical response over a range of timescales, i.e., excitation frequencies[28]. Each of the physicochemical interactions contributes to the electrode's impedance signature. If the coupling of these resistive modes can be identified, the impedance signature could be deconvolved to explicitly understand the underlying interactions. Since the timescales for these pore-scale interactions vary, their coupling differs at dissimilar frequencies, and in principle provides a consistent interpretation of geometrical characteristics from the electrochemical response.

State-of-the-art Li-ion battery composite electrodes house active material to store electrochemical energy, conductive-binder domains, CBD, ascribe (electronic) conduction pathways as well as structural rigidity and electrolyte-filled pore network ensures ionic conduction. Figure 1 (a) presents a typical RVE of such a porous electrode composed of spherical active material particles (Nickel Cobalt Manganese oxide, NCM111). The active material backbone is

stochastically generated in GeoDict[29, 30] and is consistent with particle distribution observed

experimentally[19], while the CBD phase is added in the form of physics-based description

developed recently[24] to reconstruct the composite electrode structures. Electrochemical energy is

stored in the active material particles in the form of intercalated Li. Lithium intercalation is

inherently composed of two distinct processes: (i) electrochemical reaction at the active material

– electrolyte contact, i.e., electrochemically active area; and (ii) Li diffusion inside the particle.

This jointly amounts to the faradic component of interfacial impedance (S62). In addition to this

intercalation dynamics, ionic and electronic transport experiences resistance due to finite

conductivities of the bulk phases (electrolyte and CBD) and their geometrical arrangements. The

geometrical properties such as tortuosity are obtained from pore-scale calculations on RVEs. The

RVE scale ionic impedance, z_e, and electronic impedance, z_s, are mathematically expressed in (1)

and (2). It should be recognized that z_e and z_s are not point values but rather defined over RVE

length-scale Δx, and thus measured in the units of $\Omega \cdot cm^2$. It is interesting to see that the RVE

scale ionic resistance depends on the electrolyte concentration profile that changes along the

electrode thickness, thus the electrode impedance represents a nontrivial combination of RVE scale

effects.

$$z_e(x) = \frac{-d\tilde{\phi}_e/dx \cdot \Delta x}{\tilde{I}_e} = \frac{-d\tilde{\phi}_e/dx \cdot \Delta x}{-\kappa \dfrac{\varepsilon}{\tau} \cdot d\tilde{\phi}_e/dx - \dfrac{\kappa_D}{C_e}\dfrac{\varepsilon}{\tau} \cdot d\tilde{c}_e/dx} = \frac{\Delta x}{\kappa \dfrac{\varepsilon}{\tau} + \dfrac{\kappa_D}{C_e}\dfrac{\varepsilon}{\tau} \cdot \dfrac{d\tilde{c}_e/dx}{d\tilde{\phi}_e/dx}} \qquad (1)$$

$$z_s(x) = \frac{-d\tilde{\phi}_s/dx \cdot \Delta x}{\tilde{I}_s} = \frac{-d\tilde{\phi}_s/dx \cdot \Delta x}{-\sigma^{\text{eff}} \, d\tilde{\phi}_s/dx} = \frac{\Delta x}{\sigma^{\text{eff}}} \qquad (2)$$

Here κ is ionic conductivity of the electrolyte, ε is porosity, τ is tortuosity, κ_D is diffusional

conductivity and σ^{eff} is effective electronic conductivity (effective since it accounts for both the

spatial arrangement of carbon binder domains). C_e is electrolyte concentration, ϕ_e is electrolyte phase potential (related to ionic conduction), while ϕ_s is solid phase potential (responsible for electronic conduction). Refer to Supporting Information section S3 for mathematical details. The transport properties of the electrolyte (conductivity, κ, diffusivity, D, diffusional conductivity, κ_D, and transference number, t_p) reflect the inter-ionic interactions taking place microscopically. The background solvent not only provides a medium for ions to move around and interact, but the solvent molecules also rearrange themselves around the ions and effectively act as a screening shield. The better the screening, the higher can be the salt concentration. The dielectric constant of the solvent quantifies the screening interactions[31, 32]. Thus, the electrolyte transport properties implicitly depend on the solvent's dielectric constant. Since such a solvent stabilizes the ionic charges, one expects a greater double layer capacitance.

Notice that these different physicochemical interactions have distinct length-scales. Each representative subdomain (i.e., RVE) contains multiple active material particles. The ionic and electronic conduction (i.e., transport) are long-range effects and become measurable at RVE length-scale. On the other hand, Li intercalation (reaction at the active surface and diffusion inside particles), as well as double layer charging, takes place at particle-scale (i.e., a short-range interaction). This constitutes the interfacial impedance. The current is completely ionic at electrode – separator interface. Gradually, going from separator to current collector, the charge carriers convert to electrons from ions and at the electrode – current collector interface the outgoing current is completely electronic in nature. Electrochemical reactions thus take place inside the electrode, while concurrently changing the identity of the charge carriers. At any cross-section along the electrode thickness, both ionic and electronic currents are present. Mathematically, the interfacial impedance (S63) accounts for the conversion of charge carriers as well as double layer charging/

discharging, while the ionic and electronic impedances, as defined by (1) and (2), relate to ionic and electronic conduction, respectively. If the long-range interactions were negligible, only the short-range effects dominate the electrochemical response. In this instance, the (ionic) current, I^0_{app}, flowing in from the electrode – separator interface spatially distributes as volumetric current, j. Effectively, the interfacial impedance, Z_i, at the RVE scale becomes electrode scale interfacial impedance, Z_i^L (where L is the electrode thickness):

$$Z_i^L = Z_i \big/ L \qquad (3)$$

Note that Z_i is RVE scale interfacial impedance, while Z_i^L is the measurable response at the electrode scale.

Figure 1 (b) presents the impedance response (over the frequency range 0.1 mHz to 10 kHz) of a 50 μm thick composite electrode containing 95 : 2.5 : 2.5 by weight distribution of NCM, conductive additive, and binder, respectively. The recipes considered here are consistent with the state-of-the-art electrodes[33]. The mean NCM particle radius is 5 μm and the electrode porosity is 25 % (fraction of electrode volume occupied by electrolyte-filled pores). For comparison, the electrode scale interfacial impedance (3) is also shown alongside. It appears that the interfacial impedance quite closely accounts for the larger semi-circle as well as the sloping tail. This argument is further confirmed from the phase angle (Figure 1 (d)) and impedance magnitude (Figure 1 (e)) trends for the total electrode impedance and the interfacial impedance. Over a broad range of frequencies, the interfacial impedance dominates the response, and unless further higher frequencies are probed, the long-range effects are hidden due to relatively smaller contributions at these lower frequencies. At higher frequencies (greater than 0.1 kHz), the interfacial impedance is mostly capacitive in nature (Figure 1 (d)). Since the capacitive and faradic impedances act in

parallel (A63), this reduces the magnitude of interfacial impedance considerably (Figure 1 (e)). The ionic (1) and electronic (2) resistances are present at all frequencies, and once the resistive contribution of the interfacial impedance drops, these effects appear prominently on impedance plot (Figure 1 (b)). The second semi-circular feature on the total impedance (Figure 1 (b)) is related to long-range effects, especially the ionic resistance (for this recipe 95 : 2.5 : 2.5, the electronic conductivity is fairly large; refer Figure 3 and corresponding discussion). The capacitive contribution from the electrode-electrolyte interface is still present at these frequencies and accounts for the non-zero phase angle in this higher frequency range (Figure 1 (d); purely resistive effects lead to zero phase angle). Ideally, capacitive impedance is infinite at zero frequency (a dc current) and zero at an infinite frequency (a very high-frequency ac current). Since impedance measurements are carried out in a finite frequency range, capacitive effects are present at all frequencies (hence the non-zero imaginary part). Figure 1 (e) reveals that the transport resistances are fairly greater than the interfacial impedance, which explains the smaller dimensions of the associated semi-circle (Figure 1 (b); the reactive contribution comes from the interfacial impedance and since it is smaller the highest point on the higher frequency semi-circle is at a lower height than the highest point on the low-frequency semi-circle). The electronic resistance (2) does not exhibit a frequency dependence and is constant. On the other hand, the ionic resistance (1) changes with the excitation frequency (Figure 1 (c)). Li^+ ions are the charge carriers in the electrolyte phase and their distribution (i.e., perturbation in their equilibrium distribution) changes as per expressions (S64) at different frequencies. This, in turn, affects the electrolyte phase potential distribution, dictated by expression (S66). Both these effects jointly cause the frequency dependence of ionic impedance (1).

This spatial distribution of ionic impedance (Figure 1 (c)) is thought-provoking. The ionic resistance is highest at the electrode – separator interface ($x = 0$) and gradually converges (not always monotonically) to a lower constant value at electrode – current collector interface ($x = L$) for all frequencies. This behavior is fundamentally related to interconversion of charge carriers. As the ionic current changes to the electronic, smaller current passes through the electrolyte phase, which in turn reduces the gradients in the Li^+ concentration profile and subsequently decreases the ionic resistance going towards the current collector. The solution of frequency-domain governing equations (S64) – (S66) over a range of frequencies provide quantitative values of complex impedance (Figure 1 (b)). As a part of this solution, perturbation profiles in concentrations and potentials are computed. Based on these profiles, equations (1) and (2) describe the local variation of ionic and electronic impedances. Figure 1 (c) plot the spatial variation of this ionic resistance at a few representative excitation frequencies. The electrode scale impedance sketched in the complex plane (Figure 1 (b)) is further analyzed to plot dependence of phase angle (Figure 1 (d)) and impedance magnitude (Figure 1 (e)) against excitation frequencies. Resistivity, ρ, of a bulk medium (inverse of conductivity) is measured in $\Omega \cdot cm$. Total resistance, R, is related to resistivity, ρ, as per the expression $R = \rho \ell / A$, and is measured in Ω. After rearrangement, the area specific resistance $R^* = \rho \ell$ has the units of $\Omega \cdot cm^2$. Since the discussion in Figure 1(c) (and later in Figure 2(i) and 2(j)) is in terms of area specific impedance, $\Omega \cdot cm^2$ is a suitable unit. Δx is the RVE dimension (not just a numerical parameter). Effective properties like active area, tortuosity and conductivity are computed from the pore-scale characterization of RVE sized electrode volumes. Equations (1) and (2) quantify these RVE scale impedances and correspondingly Figure 1(c) shows their distribution along the electrode thickness.

The porous electrode structure here is representative of slurry evaporation-based electrode fabrication[23]. Such an approach leads to a quite stochastic distribution of solid phases, e.g., the microstructure in Figure 1(a). Many different microstructural arrangements are possible, which in turn alters the relative features on the impedance plot[34] (Figure 1(b)) while retaining the general nature. Recently, ordered structures with ion channels are being investigated as electrode architectures[35]. The straight ion channels reduce the through-plane tortuosity and effectively ameliorates the transport limitation. For such electrodes, the impedance profile is expected to contain a very small high-frequency semi-circle. The rest of the features largely result from particle (i.e., interfacial) scale effects and probe the intercalation dynamics.

Electrode Microstructure Dictates the Impedance Components

Electrode composition correlates with effective properties such as active area and tortuosity, which in turn define different forms of microstructural resistances. Given the presence of CBD, not all the active material – electrolyte interface is available for intercalation. This reduction in active area (compared to the conventional limit of $a_0 = 3\varepsilon_s / R_p$) manifests as increased reaction overpotential, i.e., a kinetic limitation. Figure 2 (a) sketches the dependence of kinetic limitation on electrode recipe. The contours are colored as per $N_k = 1 - a / a_0$ where a is the actual active area and a_0 is the theoretical limit. At higher CBD contents, the active material surface is covered to a greater extent reducing the electrochemically active area and causing higher kinetic hindrance. Similarly, if the porosity is increased, active material volumetric loading decreases (keeping the same active material to CBD weight ratio) which in turn reduces the available area (authors have recently proved that the active material – electrolyte interface is the major contribution to active

surface, and CBD – electrolyte or active material – CBD interfaces have minor contributions to electrochemical activity[24]). Note that expression (S62) has the ratio a/a_0 as a prefactor to the charge transfer resistance. Presence of CBD also affects the electrode tortuosity. For the same porosity, increasing the CBD content reduces the pore phase tortuosity since the geometrical features associated with CBD are of smaller length scale as compared to the active material particles and makes for a relatively smoothly varying pore network[24]. The pore-scale calculations[24] were instrumental in identifying these trends as the conventionally employed relations such as the Bruggeman relation do not capture these effects arising from the presence of secondary solids. Pore network transport limitation at the RVE scale is quantified using $N_t = 1 - \varepsilon/\tau$ and sketched in Figure 2 (b). Figure 2 (b) reveals that the transport becomes effective at higher porosities (stronger dependence) and increased CBD content. The governing equations (S64) and (S66) have ε/τ as a prefactor to different ionic transport modes (diffusion and migration). Similarly, the effective electronic conductivity trends are presented in Figure 2 (c). It has been proved recently[25] that once the effective conductivity reaches 1 S/m, a major source of long-range limitations is electrolyte phase transport. In the light of this, Figure 2 (c) highlights the electrode recipes having conductivities smaller than 1 S/m. For the same CBD content (% wt.), increasing the electrode porosity decreases effective conductivity as the volumetric amount of CBD decreases and in turn cannot form strong conduction pathways. For the practical porosities, as long as CBD is present in excess of 5 % wt. and carbon to binder ratio (C/B) is 1 : 1, the electronic conduction does not become rate limiting.

Following up on this discussion, seven different electrode recipes were identified to probe the importance of the electrode composition and associated microstructural differences. The baseline recipe is 5 % wt. CBD and 25 % porosity (same as Figure 1) and all the electrodes have

identical thicknesses (50 μm). Figure 2 (d) identifies these recipes on the composition diagram along with their color codes. Figure 2 (e) compares the impedance response of these various different electrodes. By and large, their microstructural differences lead to different impedance profiles. Figure 2 (f) compares the changes in impedance behavior with CBD contents (at fixed porosity). As CBD content is increased, kinetic limitation becomes more pronounced, which results in increased interfacial impedance (Figure 2 (f)) and in turn the lower frequency semi-circle grows (Figure 2 (f) inset). Consider Figure 2 (g) which explores the porosity variation. Increased porosity reduces the ionic resistance (Figure 2 (g)) as tortuosity decreases. This reflects as the impedance profile moves closer to the origin (Figure 2 (g) inset). When both the CBD content and porosity are increased, the effect on the impedance response is cumulative (Figures 2 (h) and (i)). Increased CBD content explains the higher interfacial impedance (Figure 2 (h)) given higher coverage of the active material surface. This also explains the impedance growth in the lower frequency semi-circle (Figure 2 (h) inset). In addition to this, increased porosity reduces the ionic resistance (Figure 2 (i)). This features as the electrode impedance profile moving closer to the origin (Figure 2 (h) inset). Thus, electrode impedance is strongly associated with microstructural arrangements (i.e., electrode recipe). In other words, a specific recipe leads to certain microstructural arrangements which translate into different contributions from short- and long-range limitations. Figure 2 (j) sketches these recipes on transport vs. interfacial impedance contribution map (high-frequency impedance is dissected for this figure). It quantitatively summarizes the origins of electrode impedance (at the highest frequency – 10 kHz). Electrode scale interfacial resistance is estimated from (3), while the ionic and electronic contributions are related to their local variation as per the following expressions:

$$Z_e^L = \sum z_e \tag{4}$$

$$Z_s^L = \sum z_s \tag{5}$$

Here summation is carried out over all the sub-volumes constituting the electrode thickness. Note that all these quantities (including Z_i^L) have identical units of $\Omega \cdot cm^2$ and allows for a direct comparison. As CBD content is increased, the interfacial contributions grow and accordingly the data points move closer to the equal contribution line (at 45°). With porosity changes, the transport resistance diminishes and in turn symbols show the increased contribution from interfacial effects. When both CBD content and porosity are increased, kinetic limitation grows, and transport limitations diminish concurrently, leading to the highest shift (among the recipes studied) in corresponding behavior in Figure 2 (j).

It has been sown earlier that the CBD phase exhibits the highest conductivity near the C/B ratio of 1[14, 15]. Hence this C/B ratio is used for the most part. If the conductive additives are reduced, effective electronic conductivity drops and which in turn makes the solid-state conduction limitations more prominent. As discussed earlier, these long-range limitations alter the high-frequency response. Figure 3 (a) shows the change in impedance response with a reduction in C/B ratio while keeping other phases invariant (i.e., 95 % wt. active material and 25 % porosity). Figure 3 (b) reports the relative contribution of different mechanisms to the total impedance at the highest frequency studied here, i.e., 10 kHz. It appears that once the C/B ratio drops below 0.5, appreciable electronic conduction limitations arise. This is an interesting observation as a smaller C/B ratio (in the range 0.5 to 1.0) allows one to use more binder to improve structural rigidity as well as accommodate intercalation stresses without detrimentally altering the electronic conduction. In line with this discussion, Figure 2 (c) would change considerably once the C/B ratio becomes

smaller than 0.5. Note that Figure 3 (a) uses logarithmic axes in order to sufficiently delineate the high-frequency signature of the C/B ratio.

Pore-scale Resistances translate Non-monotonically to Electrode-scale

Recent years have seen increased efforts towards enabling the thick electrode technology, however, the fundamental origins for underutilization remain unclear[13, 36-38]. Approaches like reduced particle size[36] or graded electrodes[38] are proposed with marginal improvement in performance. The composite electrodes exhibit complexations associated with the presence of multiple phases. Expressions (3), (4) and (5) suggest that the pore-scale interactions resulting in an electrochemical response of an electrode do not scale identically. To further probe this spatial coupling and associated speciation, impedance behavior of electrodes with different thicknesses is probed in Figure 4. These electrodes have identical microstructural arrangements (same as the baseline) and only their thicknesses are varied from 25 μm (thin) to 200 μm (thick) electrode. Figures 4 (a) and (b) show their respective (area specific) impedances. Curious trends are observed here. Increasing electrode thickness from 25 μm to 100 μm (Figure 4 (a)) shows a decrease in the overall impedance behavior, while at further higher thicknesses (100 to 200 μm; Figure 4 (b)) the impedance grows, though this growth is much slower in comparison to the initial drop. Additionally, the higher frequency semi-circle that reflects the transport limitations grows steadily as the thickness is increased from 25 to 200 μm. At higher thicknesses (125 μm and above; Figure 4 (b)), it merges with the lower frequency semi-circle and one cannot visually isolate the two.

As the electrode volumes increase with increasing thickness, a comparison based on area specific impedance does not seem appropriate. Impedance data is rescaled to obtain volume

specific impedance $\left(Z^{*} = Z \cdot L \right)$, and the corresponding profiles are shown in Figure 4 (c). Figure 4 (c) reveals a clear monotonic trend. As intuitively expected, the impedance grows with electrode thickness. Also, the gradual reduction in lower frequency semi-circle (related to the short-range effects) and impedance build up in the high-frequency semi-circle (describes the long-range interactions) are clearly demarcated. Figure 4 (d) compares the contributions of these various physicochemical interactions with electrode thickness (volume specific impedance values are employed) at a certain higher frequency (10 kHz here). Such a behavior sheds light on the spatial coupling of these interactions. As the incoming current distributes locally to form the intercalation and capacitive current, the overall effect of the interfacial impedance felt at the electrode scale diminishes with increased electrode thickness. On the other hand, the transport resistances act in series and in turn their magnitude grows with thickness. Expressions (3) to (5) mathematically highlight these behavioral differences among the interfacial (short-range) and transport (long-range) effects. Reconsider Figure 4 (d). For thin electrodes, the kinetics is the limiting contribution and accordingly the strategies that increase the active area lead to better performance[24]. For thick electrodes, transport becomes the rate limiting factor and consequently, the same strategies as before would not result in considerable improvement. Appropriate microstructural modifications that lead to improved thick electrode behavior are required. To the best of authors' knowledge, there is only one careful experimental study (Ogihara *et al.*[39]) that compares impedance response as a function of electrode thickness and finds qualitatively similar trends as Figure 4 (a). However, given their circuit-based interpretation, fundamental mechanisms leading to such a response could not be identified[39]. The physics-based impedance analysis presented here consistently connects pore-scale events to electrode-scale and provides new insights.

Impedance Response of Multivalent Chemistries

Lithium (Li^+) is a monovalent cation. With depleting lithium reserves, various other cations, for example, magnesium (Mg^{2+}), aluminum (Al^{3+}) are being considered. Two distinct effects become relevant as these multivalent cations are considered. First, for the same current, lesser atoms intercalate which reduces the diffusional impedance and in turn slope of the low-frequency tail increases. Second, the transference number increases in the electrolyte which amounts to reduced transport resistance. Figures S2 sketches these representative differences, assuming all the kinetic and transport properties to be identical. In reality, whenever a new cation is considered for electrochemistry, intercalation host, electrolyte etc. are revised. Many of these intercalation hosts undergo multiphase intercalation[40, 41] which requires a reformulation of interfacial resistance. However, even in the absence of these material nonlinearities, the impedance response varies nonmonotonically given the direct relation of cationic charge with diffusional flux and electrolyte transference.

Conclusions

State-of-the-art porous electrodes are a multiphase system with each phase aimed at improving a specific physicochemical interaction. Impedance spectroscopy is often used to characterize the electrochemical response of such electrodes, but the traditionally employed equivalent circuit-based interpretation offers rather qualitative insights.

This work develops a consistent description of the electrochemical impedance of composite porous electrodes. Such an account correlates various impedance features to relevant pore-scale events as well as effective microstructural properties. Frequency dependence of impedance can be

interpreted in terms of timescales. Based on the time scale (i.e., probing frequency), these interactions couple differently. It is found that even for a moderate size electrode ($\sim 50\ \mu m$) if large enough excitation frequencies are employed, the transport limitations appear as a second semi-circle on the impedance spectra (in addition to the lower frequency semi-circle associated with interfacial short-range effects).

The choice of electrode recipe uniquely identifies the spatial arrangement of the material phases constituting these electrodes and positively alters the impedance response. Specifically, when CBD weight fraction (active material and CBD are the solid phases) is increased, it reduces the available intercalation area and in turn, the lower frequency impedance grows. On the other hand, porosity variations lead to changes in the transport resistance. Interestingly, the CBD weight fraction also changes the tortuosity (and in turn high-frequency impedance) at the same porosity, and porosity changes affect the lower frequency impedance. These secondary effects are a result of the composite electrode structure.

As the length-scales of these different interactions are different as well as their spatial coupling, changes in electrode thickness do not scale these interactions identically. With increased electrode thickness, the contribution of interfacial impedance decreases, and the transport effects become more pronounced which leads to appropriate changes in the respective semi-circles. For thick enough electrodes, both the semi-circles merge as the transport effects become activated at lower frequencies.

Supporting Information includes the following:
1. Concentrated Solution Theory based Electrolyte Transport Description
2. Electrochemical Response of a Double Layer
3. Mathematical Details of Electrode Impedance
4. Impedance for Multivalent Intercalation Chemistry

Acknowledgments

References

1.   E. J. Cairns and P. Albertus, *Annu. Rev. Chem. Biomol. Eng.*, 2010, **1**, 299-320.
2.   M. Armand and J.-M. Tarascon, *Nature*, 2008, **451**, 652-657.
3.   V. Etacheri, R. Marom, R. Elazari, G. Salitra and D. Aurbach, *Energy Environ. Sci.*, 2011, **4**, 3243-3262.
4.   B. Dunn, H. Kamath and J.-M. Tarascon, *Science*, 2011, **334**, 928-935.
5.   F. T. Wagner, B. Lakshmanan and M. F. Mathias, *J. Phys. Chem. Lett.*, 2010, **1**, 2204-2219.
6.   K. Xu, *Chem. Rev.*, 2014, **114**, 11503-11618.
7.   S. Ahmed, I. Bloom, A. N. Jansen, T. Tanim, E. J. Dufek, A. Pesaran, A. Burnham, R. B. Carlson, F. Dias and K. Hardy, *J. Power Sources*, 2017, **367**, 250-262.
8.   A. Meintz, J. Zhang, R. Vijayagopal, C. Kreutzer, S. Ahmed, I. Bloom, A. Burnham, R. B. Carlson, F. Dias and E. J. Dufek, *J. Power Sources*, 2017, **367**, 216-227.
9.   J.-M. Tarascon and M. Armand, *Nature*, 2001, **414**, 359-367.
10.   J. B. Goodenough and K.-S. Park, *J. Am. Chem. Soc.*, 2013, **135**, 1167-1176.
11.   H. Zheng, L. Tan, G. Liu, X. Song and V. S. Battaglia, *J. Power Sources*, 2012, **208**, 52-57.
12.   H. Zheng, G. Liu, X. Song, P. Ridgway, S. Xun and V. S. Battaglia, *J. Electrochem. Soc.*, 2010, **157**, A1060-A1066.
13.   H. Zheng, J. Li, X. Song, G. Liu and V. S. Battaglia, *Electrochim. Acta*, 2012, **71**, 258-265.
14.   H. Zheng, R. Yang, G. Liu, X. Song and V. S. Battaglia, *J. Phys. Chem. C*, 2012, **116**, 4875-4882.
15.   G. Liu, H. Zheng, X. Song and V. S. Battaglia, *J. Electrochem. Soc.*, 2012, **159**, A214-A221.
16.   L. Zielke, T. Hutzenlaub, D. R. Wheeler, I. Manke, T. Arlt, N. Paust, R. Zengerle and S. Thiele, *Adv. Energy Mater.*, 2014, **4**, 1301617.
17.   L. Zielke, T. Hutzenlaub, D. R. Wheeler, C. W. Chao, I. Manke, A. Hilger, N. Paust, R. Zengerle and S. Thiele, *Adv. Energy Mater.*, 2015, **5**, 1401612.
18.   G. J. Nelson, L. J. Ausderau, S. Shin, J. R. Buckley, A. Mistry, P. P. Mukherjee and V. De Andrade, *J. Electrochem. Soc.*, 2017, **164**, A1412-A1424.
19.   M. Ebner, F. Geldmacher, F. Marone, M. Stampanoni and V. Wood, *Adv. Energy Mater.*, 2013, **3**, 845-850.
20.   O. O. Taiwo, D. P. Finegan, D. S. Eastwood, J. L. Fife, L. D. Brown, J. A. Darr, P. D. Lee, D. J. Brett and P. R. Shearing, *J. Microsc.*, 2016, **263**, 280-292.
21.   P. Shearing, N. Brandon, J. Gelb, R. Bradley, P. Withers, A. Marquis, S. Cooper and S. Harris, *J. Electrochem. Soc.*, 2012, **159**, A1023-A1027.

22.   O. O. Taiwo, D. P. Finegan, J. Gelb, C. Holzner, D. J. Brett and P. R. Shearing, *Chem. Eng. Sci.*, 2016, **154**, 27-33.
23.   M. Stein, A. Mistry and P. P. Mukherjee, *J. Electrochem. Soc.*, 2017, **164**, A1616-A1627.
24.   A. N. Mistry, K. Smith and P. P. Mukherjee, *ACS Appl. Mater. Interfaces*, 2018, **10**, 6317-6326.
25.   A. Mistry, D. Juarez-Robles, I. V. M. Stein, K. Smith and P. P. Mukherjee, *J. Electrochem. Energy Convers. Storage*, 2016, **13**, 031006-031006.
26.   P. Pietsch and V. Wood, *Annual Review of Materials Research*, 2017.
27.   A. N. Mistry, K. Smith and P. P. Mukherjee, *ACS Appl. Mater. Interfaces*, 2018, **10**, 28644-28655.
28.   C. T. Love, M. B. V. Virji, R. E. Rocheleau and K. E. Swider-Lyons, *J. Power Sources*, 2014, **266**, 512-519.
29.   GeoDict (http://www.geodict.com/).
30.   A. Wiegmann, GEODICT: virtual microstructure simulator and material property predictor (http://www.geodict.com/).
31.   P. Atkins, J. De Paula and J. Keeler, *Atkins' physical chemistry*, Oxford university press, 2018.
32.   J. N. Israelachvili, *Intermolecular and surface forces*, Academic press, New York, 2011.
33.   T. Marks, S. Trussler, A. Smith, D. Xiong and J. Dahn, *J. Electrochem. Soc.*, 2011, **158**, A51-A57.
34.   S. Cho, C.-F. Chen and P. P. Mukherjee, *J. Electrochem. Soc.*, 2015, **162**, A1202-A1214.
35.   C.-J. Bae, C. K. Erdonmez, J. W. Halloran and Y.-M. Chiang, *Adv. Mater.*, 2013, **25**, 1254-1258.
36.   Z. Du, D. L. Wood, C. Daniel, S. Kalnaus and J. Li, *J. Appl. Electrochem.*, 2017, **47**, 405-415.
37.   T. Danner, M. Singh, S. Hein, J. Kaiser, H. Hahn and A. Latz, *J. Power Sources*, 2016, **334**, 191-201.
38.   Y. Qi, T. Jang, V. Ramadesigan, D. T. Schwartz and V. R. Subramanian, *J. Electrochem. Soc.*, 2017, **164**, A3196-A3207.
39.   N. Ogihara, Y. Itou, T. Sasaki and Y. Takeuchi, *J. Phys. Chem. C*, 2015, **119**, 4612-4619.
40.   L. R. De Jesus, J. L. Andrews, A. Parija and S. Banerjee, *ACS Energy Lett.*, 2018, **3**, 915-931.
41.   J. L. Andrews, A. Mukherjee, H. D. Yoo, A. Parija, P. M. Marley, S. Fakra, D. Prendergast, J. Cabana, R. F. Klie and S. Banerjee, *Chem*, 2018, **4**, 564-585.

List of Figures

		the highest frequency – 10 kHz. Marked changes are observed when the carbon to binder ratio drops below 5:10 wt. Since the logarithmic axis is used on the impedance plot to express this effect, spectra are visually different than the other figures.
	4	The RVE scale impedance contributions scale differently at electrode scale. (a) and (b) Area-specific impedance gives non-monotonic progression with electrode thicknesses highlighting this non-linear scaling of pore-scale physicochemical interactions. On the other hand, the trends become clearer when volume specific impedances (c) are plotted. The lowest thickness electrode shows two clear semi-circles, the lower frequency one corresponding to charge transfer kinetics and the higher frequency one related to transport effects. As electrode thickness is increased, the two semi-circles merge and for thicker electrodes, only one semi-circle is observed. (d) Relative contributions from interfacial, ionic and electronic impedances are characterized at the highest excitation frequency – 10 kHz and reveal that the long-range transport effects become prominent as electrode thickness is increased. All these electrodes have 95 % wt. active material (i.e., 5 % wt. CBD) and 25 % porosity. As the CBD phase content is fairly sufficient to provide conduction pathways (Figure 2 (c)), impedance contribution of the electronic mode is minimal in (d).

Figure 1: Electrochemical impedance response of a 50 μm thick porous composite electrode having 25% porosity and 95 : 2.5 : 2.5 %wt. composition with spherical active material particles. (a) An RVE of such electrode is shown along with all the constituents; (b) Corresponding electrode impedance response and contribution of the interfacial impedance at electrode scale; (c) Ionic resistance (Eq. 1) trends at different excitation frequencies ($x = 0$ is electrode – separator interface, while $x = L$ is electrode – current collector boundary); (d) and (e) comparison between total electrode impedance and interfacial impedance at the electrode scale in terms of phase angle and magnitudes, respectively. The impedance of a porous intercalation electrode relies on (a) electrode microstructure, i.e., the spatial arrangement of different material phases. Given that, the electrode scale impedance (b) is an outcome of spatial coupling of short-range (i.e., interfacial (b)) and long-range (e.g., ionic transport (c)) interactions. (d) Phase angle quantifies the relative contribution of resistive and capacitive effects. (e) Impedance decreases with the frequency of excitation.

Figure 2: Role of electrode recipe on impedance is intricate as physicochemical interactions scale differently with microstructural specifications. (a), (b) and (c) present dependence of kinetic, transport and electronic conduction limitations on electrode recipe, respectively. Kinetic

limitations are associated with a reduction in the electrochemically active area. Electrolyte phase transport effects are correlated with porosity and tortuosity. (c) Electrodes have appreciable electronic conductivity as long as the conductive binder phase is present in excess of 5 % wt. (conductive additives to binder ratio is 1:1 by weight; effect of their relative amounts is explored in Fig. 3). Seven different electrode recipes (d) are studied in terms of respective impedance spectra (e). (f) Increasing the CBD phase loading results in the reduced active area and in turn greater interfacial impedance. (g) The porosity changes alter the electrolyte transport resistance. A simultaneous change, on the other hand, alters both the (h) interfacial as well as (i) transport effects. Insets show corresponding electrode impedance spectra comparisons, over the frequency range 0.1 mHz to 10 kHz. Representative frequencies (f), (g) and (h) are shown for the inflection point where diffusional impedance connects to the kinetic semi-circle and the highest imaginary impedance point on the kinetic semi-circle. (j) The microstructural differences across these recipes manifest as varying relative contributions from transport and interfacial effects. The relative contributions are assessed at the highest frequency – 10 kHz.
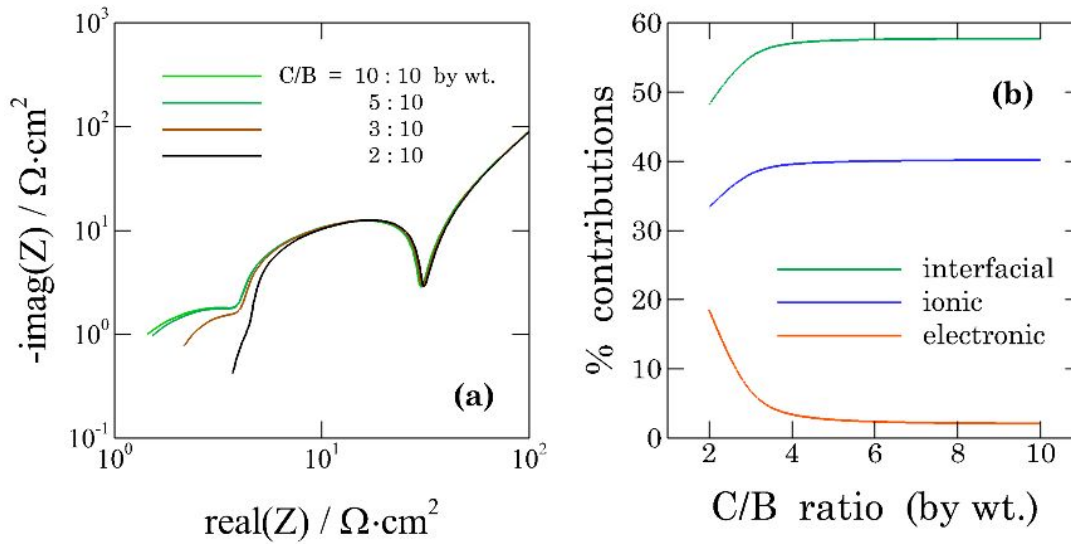
Figure 3: Effect of carbon – to – binder ratio (C/B) on electrode impedance at constant porosity (25%) and active material loading (95 %wt.). Electronic conductivity varies with C/B ratio and in turn impedance response (a) changes, especially at higher frequencies when long-range limitations are dominant. (b) Relative contributions of interfacial, ionic and electronic components are assessed at the highest frequency – 10 kHz. Marked changes are observed when the carbon to binder ratio drops below 5:10 wt. Since the logarithmic axis is used on the impedance plot to express this effect, spectra are visually different than the other figures.
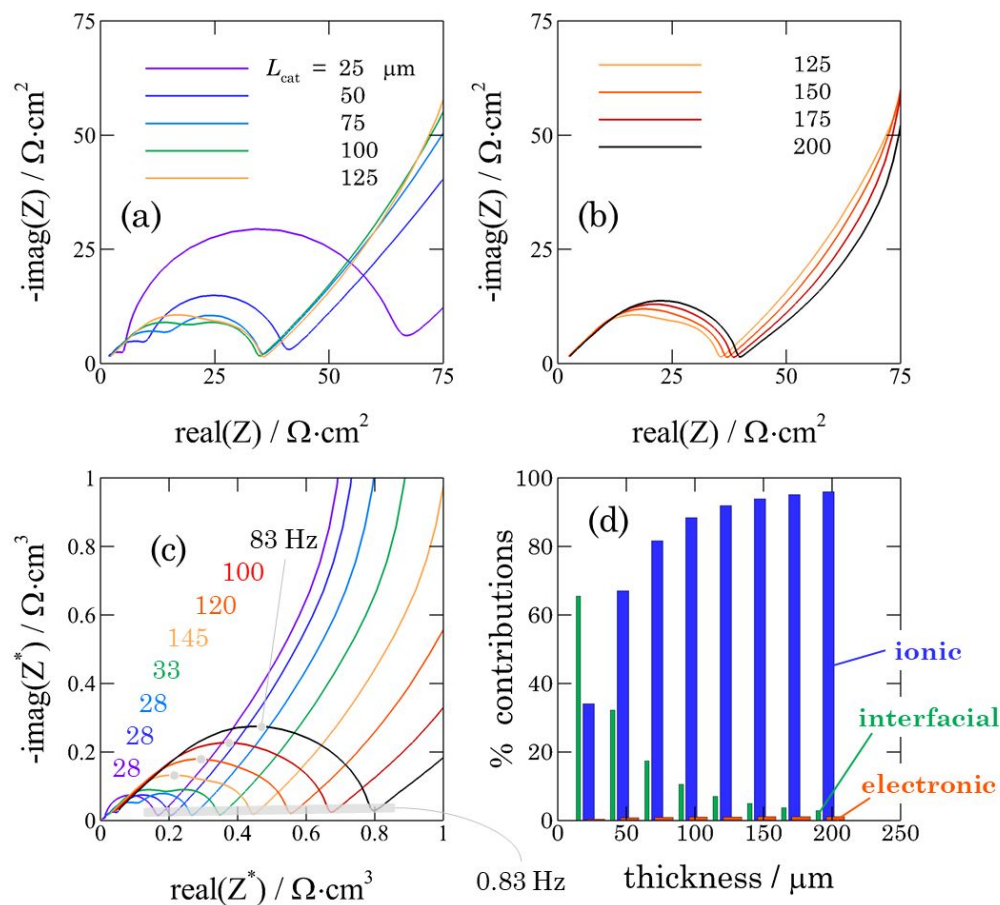
Figure 4: The RVE scale impedance contributions scale differently at electrode scale. (a) and (b) Area-specific impedance gives non-monotonic progression with electrode thicknesses highlighting this non-linear scaling of pore-scale physicochemical interactions. On the other hand, the trends become clearer when volume specific impedances (c) are plotted. The lowest thickness electrode shows two clear semi-circles, the lower frequency one corresponding to charge transfer kinetics and the higher frequency one related to transport effects. As electrode thickness is increased, the two semi-circles merge and for thicker electrodes, only one semi-circle is observed. (d) Relative contributions from interfacial, ionic and electronic impedances are characterized at the highest excitation frequency – 10 kHz and reveal that the long-range transport effects become prominent as electrode thickness is increased. All these electrodes have 95 % wt. active material (i.e., 5 % wt. CBD) and 25 % porosity. As the CBD phase content is fairly sufficient to provide conduction pathways (Figure 2 (c)), impedance contribution of the electronic mode is minimal in (d).

Graphical Abstract
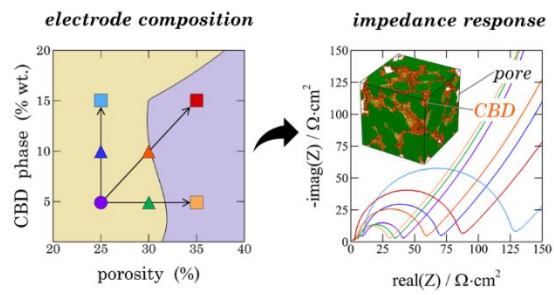
Novelty of work. The spatial coupling between the pore-scale microstructural resistances and the electrode-scale measurements is detailed via a physics-based, mechanistic description.